Materials and Design 199 (2021) 109390

Contents lists available at ScienceDirect

Materials and Design

journal homepage: www.elsevier.com/locate/matdes

Inverse design of topological metaplates for flexural waves with machine learning

Liangshu He [a,1], Zhihui Wen [a,1], Yabin Jin [a,*], Daniel Torrent [b], Xiaoying Zhuang [c,d], Timon Rabczuk [e]

[a] School of Aerospace Engineering and Applied Mechanics, Tongji University, 200092 Shanghai, China
[b] GROC-UJI, Institut de Noves Tecnologies de la Imatge, Universitat Jaume I, 12080 Castello, Spain
[c] Department of Geotechnical Engineering, College of Civil Engineering, Tongji University, 200092 Shanghai, China
[d] Institute of Photonics, Department of Mathematics and Physics, Leibniz University Hannover, Germany
[e] Institute of Structural Mechanics, Bauhaus-Universität Weimar, Weimar D-99423, Germany

HIGHLIGHTS

- The trained neural network directly connects the bandgap characteristics with the geometric parameters.
- The neural network finds out the object parameters accurately for inversely designing topological edge states.
- Multiple scattering method is applied to simulate the direction selective topological edge states with wide bandgap.
- The inverse design method has great potential applications for signal processing, sensing, and energy harvesting.

GRAPHICAL ABSTRACT

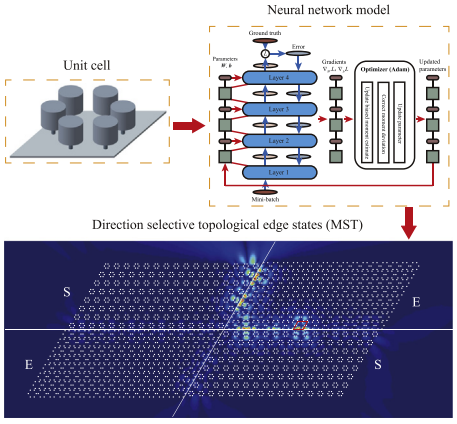

ARTICLE INFO

Article history:
Received 11 October 2020
Received in revised form 20 November 2020
Accepted 29 November 2020
Available online 8 December 2020

ABSTRACT

The mechanical analog to the topological insulators brings anomalous elastic wave properties which diversifies classic wave functions for potential broad applications. To obtain topological mechanical wave states with good quality at desired frequency ranges, it needs repetitive trials of different geometric parameters with traditional forward designs. In this work, we develop an inverse design of topological edge states for flexural wave using machine learning method which is promising for instantaneous design. Nonlinear mapping function from input targets to output desired parameters are adopted in artificial neural networks where the data sets for training are generated by the plane wave expansion method. Topological edge states are then realized and compared for different bandgap width conditions with such inverse designs, proving that wide bandgap can promote the confinement of the topological edge states. Finally, direction selective propagations with sharp turns are further demonstrated as anomalous wave behaviors. The machine learning inverse design of topological states for flexural wave provides an efficient way to design practical devices with targeted needs for potential applications such as signal processing, sensing and energy harvesting.

* Corresponding author.
E-mail address: 083623jinyabin@tongji.edu.cn (Y. Jin).
[1] Equal contribution.

https://doi.org/10.1016/j.matdes.2020.109390

1. Introduction

Topological insulators are an emerging topic in condensed matter physics [1–3] that can provide anomalous properties like direction selective propagation, back scattering free and high robustness. In recent years, it has been successfully extended to classical systems such as photonics [4–7], plasmonics [8,9], acoustics [10–13] and mechanics [14,15], boosting the development of new manipulations for classical waves. When confined in elastic plates, mechanical waves present three polarizations, also named the symmetric (S), shear-horizontal (SH) and antisymmetric (or flexural) modes. In the low frequency limit, the S and SH modes present a linear dispersion relation while the flexural mode has a parabolic dispersion [16,17]. The mechanical analogs to the quantum spin Hall effect and the quantum valley Hall effect have been applied mainly to the flexural mode to design topologically protected states in nontrivial bandgaps opened from Dirac cones [18–20].

The original Dirac frequency and the width of the opened nontrivial bandgap are the two main parameters to design the topological states. Most works in the literature reported a forward design approach where certain geometric parameters are firstly chosen and then followed by the computation of the Dirac frequency and the opened bandgap. However, from application point of view, it is more likely to be given a desired frequency and bandgap width, and then the goal is to find out what are the geometric parameters to achieve the topological states. Such a process belongs to an inverse design approach. It should be noted that topological edge states will infiltrate into the bulk structures widely or even disappear if the bandgap width is too small. Such problem can be better handled through an inverse design strategy with constraints on the bandgap with, so that it can be used to solve this issue.

Nowadays, based on optimization techniques, many popular algorithms are used in the inverse design such as topology optimization [21,22], genetic algorithm [23], particle swarming optimization [24], among others. With desired functions, these algorithms develop a space with full parameters and then obtain nonmonotonic designs, being an obvious advantage of these techniques. Inspired by the neural networks in biology, artificial neural networks have revolutionized many disciplines in science and engineering, or even in art and literature. The subfield machine learning technique can work in a smarter strategy by data-driven learning to provide a solution instantaneously with a best fit of the needed performance. Machine learning technique has been considered an excellent candidate for the inverse design of nanophotonic [25–27], plasmonics [28,29], metamaterials [28], metasurfaces [30]. Recently, it is also reported machine learning inverse design for acoustic imaging [31], band structure [32], cluster topological phononics [33], plate's vibration analysis [34–36], and so on.

In this work, machine learning technique is adopted to inversely design a metaplate to achieve topological edge states for flexural wave. In the employed artificial neural network, continuous mapping function from input vector to output vector is highly nonlinear and its information processing ability comes from the multiple compounding of linear functions. The metaplate consists of honeycomb arrangement of resonators deposited on a thin elastic plate. Two neural networks are established for the forward and the backward prediction of bandgap width and the geometric parameters. Topological edge states are further designed and the influence of the bandgap width is detailed discussed, which help to realize directional selective propagation in a complex cross structure. The outline of the work is as follows: After the introduction in this section, we introduce the plane wave expansion method (PWE) to calculate the dispersion relation and the Dirac frequency of the metaplates in Section 2; In Section 3, we employ the PWE method to generate sufficient data sets, then establish two neural networks for the forward and the backward prediction of bandgap width and geometric parameters; In Section 4, we use the trained neural network to predict the resonators arrangement parameter with different desired bandgap widths and further construct topological edge state modes; In Section 5, we demonstrate the designed topological edge states with multiple scattering simulation; Finally we summarize this work in Section 6.

2. Methodology of the meta-plate

In this section, we briefly introduce the classical thin plate theory for flexural wave propagation and describe the methodology. The considered meta-plate unit is placed in Fig. 1(b), consisting of six resonators connected to a thin aluminum plate through thin necks. The resonators are designed in a honeycomb lattice, as shown by the blue dots in Fig. 1(a). Two kinds of unit cells, namely the blue and red units, contain two and six resonators, respectively, with their corresponding Brillouin zones shown at right. We set the thickness of the metal aluminum plate h to 1 mm ($E = 77.6$ GPa, Poisson ratio $\nu = 0.352$ and density $\rho = 2730$ Kgm^{-3}) with a lattice constant $a = 50$ mm. The resonator neck is made of plastic with $h_{neck} = 1.5$ mm and $d_{neck} = 2$ mm ($E_{neck} = 3.2$ GPa, Poisson ratio $\nu_{neck} = 0.35$ and density $\rho_{neck} = 1190$ Kgm^{-3}). The resonator head is made of tungsten alloy ($E_{head} = 334.6$ GPa, $\nu_{head} = 0.28$ and $\rho_{head} = 19{,}260$ Kgm^{-3}) with $h_{head} = 44$ mm and $d_{head} = 8$ mm.

According to Kirchhoff plate theory, the equation of motion for flexural waves in the meta-plate can be written as [37].

$$\left(D\nabla^4 - \omega^2\rho h\right)w(\boldsymbol{r}) = \sum_{\boldsymbol{R}_i,\,\alpha}\omega^2 m_R w_1(\boldsymbol{R}_{i\alpha})\delta(\boldsymbol{r}-\boldsymbol{R}_{i\alpha}) \tag{1}$$

where $D = Eh^3/12(1-\nu^2)$ represents the flexural stiffness of the plate, ∇^4 the biharmonic operator, $\boldsymbol{r} = (x,y)$ the position vector of any point on the plate, ω the angular frequency and w is the out-of-plane displacement. The position of the resonators in each honeycomb lattice can be described as $\boldsymbol{R}_{i\alpha} = \boldsymbol{R}_i + \boldsymbol{R}_\alpha$, where i runs for all the direct lattice vectors and α runs for all the six resonators within the unit cell. The resonator and the neck can be simplify regarded as a mass $m_R = \pi d^2_{head} h_{head}/4$ and a linear spring with a stiffness constant $k_\alpha = \pi E_{neck} d^2_{neck}/4h_{neck}$, respectively [19]. According to Newton's second law and the coordination equation of the lattice, the equation of motion for each resonator is

$$\omega^2 m_R w_1(\boldsymbol{R}_{i\alpha}) = -k_{n\alpha}(w(\boldsymbol{R}_{i\alpha}) - w_1(\boldsymbol{R}_{i\alpha})) \tag{2}$$

The solution for the displacement field w can be expanded using Bloch theorem as

$$w(\boldsymbol{r}) = \sum_{\boldsymbol{G}} w(\boldsymbol{G})\, e^{-j(\boldsymbol{G}+\boldsymbol{K})\cdot\boldsymbol{r}} \tag{3}$$

where $\boldsymbol{K}$ denotes the Bloch wave number and $\boldsymbol{G} = m\boldsymbol{g}_1 + n\boldsymbol{g}_2$ the reciprocal lattice vector, m and n are integers, $\boldsymbol{g}_1$ and $\boldsymbol{g}_2$ are basis vectors of the reciprocal lattice which can be used to define the corresponding Brillouin zones, as shown in Fig. 1(a). The basis vectors of honeycomb lattice $\boldsymbol{a}_i$ and the reciprocal lattice satisfy [38].

$$\boldsymbol{a}_i \cdot \boldsymbol{g}_j = 2\pi\delta_{ij}\,(i,j = 1,2)$$

The quasi-periodicity condition of the displacement field imposed by Bloch theorem implies

$$w_1(\boldsymbol{R}_\alpha) = w_1(\boldsymbol{R}_\alpha(0))\, e^{-j\boldsymbol{K}\cdot\boldsymbol{R}_\alpha} \tag{4}$$

Then the equation of motion in Eq. (1) can be expressed as

$$\left(\nabla^4 - \omega^2\rho h/D\right)w(\boldsymbol{r}) = \sum_{\boldsymbol{R}_i}\sum_{\alpha} t_\alpha w_1(\boldsymbol{R}_{i\alpha})\delta(\boldsymbol{r}-\boldsymbol{R}_{i\alpha}) \tag{5}$$

where $\nabla^4 = ((\boldsymbol{k}_x + \boldsymbol{G}_x)^2 + (\boldsymbol{k}_y + \boldsymbol{G}_y)^2)^2$, $\boldsymbol{K}=[\boldsymbol{k}_x, \boldsymbol{k}_y]$ and $\boldsymbol{G}=[\boldsymbol{G}_x, \boldsymbol{G}_y]$. Here, t_α is the stiffness coefficient of the meta-plate defined as

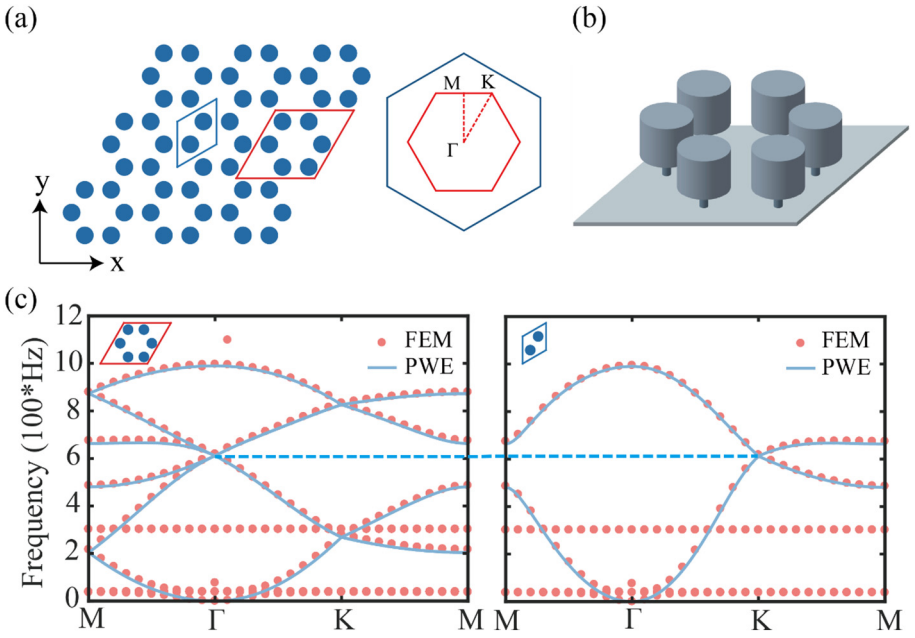

Fig. 1. (a) Two unit-cell representations and the corresponding Brillouin zones on the right. (b) A diagrammatic sketch of the red unit cell with six resonators of the meta-plate. (c) Dispersion curves of the meta-plate with unit cells contain six resonators (see the inset in the left panel) and two resonators (see the inset in the right panel), respectively, are calculated by the PWE and the FEM methods. Additional modes appearing in FEM calculation are shear-horizontal and shear plate modes and bending modes. Double Dirac cones at Γ point and single Dirac cone at K point are marked by horizontal dashed line.

$$t_\alpha = \frac{\gamma_\alpha S(\Omega a)^2}{a^4\left(1-(\Omega a)^2/(\Omega_\alpha a)^2\right)} \tag{6}$$

where $S=\sqrt{3}a^2/2$ is the area of the honeycomb unit cell, $\Omega^2=\omega^2\rho a^2 h/D$ is the normalized frequency, $\gamma=m_R/(\rho Sh)$ the normalized mass and $\Omega_\alpha^2=k_{n\alpha}\rho a^2 h/m_{n\alpha}D$ is the normalized resonant frequency of each resonator.

By combining the above equations with algebraic operations, we can obtain the governing equations of the meta-plate as follows:

$$\begin{vmatrix} 1-\Psi_{11} & -\Psi_{12} & -\Psi_{13} & -\Psi_{14} & -\Psi_{15} & -\Psi_{16} \\ -\Psi_{21} & 1-\Psi_{22} & -\Psi_{23} & -\Psi_{24} & -\Psi_{25} & -\Psi_{26} \\ -\Psi_{31} & -\Psi_{32} & 1-\Psi_{33} & -\Psi_{34} & -\Psi_{35} & -\Psi_{36} \\ -\Psi_{41} & -\Psi_{42} & -\Psi_{43} & 1-\Psi_{44} & -\Psi_{45} & -\Psi_{46} \\ -\Psi_{51} & -\Psi_{52} & -\Psi_{53} & -\Psi_{54} & 1-\Psi_{55} & -\Psi_{56} \\ -\Psi_{61} & -\Psi_{62} & -\Psi_{63} & -\Psi_{64} & -\Psi_{65} & 1-\Psi_{66} \end{vmatrix} = 0 \tag{7}$$

where

$$\Psi_{\alpha\beta} = \frac{t_\alpha a^4}{S}\sum_{\boldsymbol{G}} \frac{e^{-\boldsymbol{G}\cdot\boldsymbol{R}_{\alpha\beta}}}{\left((\boldsymbol{k}_x+\boldsymbol{G}_x)^2+(\boldsymbol{k}_y+\boldsymbol{G}_y)^2\right)^2 a^4-(\Omega a)^2} \tag{8}$$

Eq. (7) defines a secular equation from which we can obtain the frequency as a function of the Bloch wave vector $\boldsymbol{K}$, where it is convenient to define the frequency f as

$$f = \frac{\Omega}{2\pi a}\sqrt{\frac{\rho h}{D}} \tag{9}$$

We solve the eigenvalue problem analytically with the PWE method and numerically with finite element method (FEM) and plot the dispersion curves in Fig. 1(c). The dispersion diagrams with the red and blue units in Fig. 1(a) are shown in the left and right panels, respectively. The band structure of flexural modes from FEM and PWE methods are highly consistent. The additional modes obtained from the FEM method correspond to the other plate's modes and resonator's modes. It is clearly observed that the dispersions of the fundamental flexural modes of the meta-plates are typically parabolic in the low frequency limit. The double Dirac cones at Γ point in the left panel and the single Dirac cone at K point in the right panel have the same frequency $f_D = 611.5$ Hz, as marked by the blue dotted line. In fact, the double Dirac cones originate from the zone-folding effect of band structures [19]. Therefore, the frequency of the double Dirac cones can be described by the frequency of the single Dirac cone.

For the blue unit with double resonators in Fig. 1(a), Eq. (7) can be easily simplified as

$$\begin{vmatrix} 1-\Psi_{11} & -\Psi_{12} \\ -\Psi_{21} & 1-\Psi_{22} \end{vmatrix} = 0 \tag{10}$$

The above secular equation can also be expanded for low $\boldsymbol{k}$ around the Dirac point K, and then a conical dispersion curve is found, defining therefore a Dirac cone whose speed and frequency can be found both numerical or analytically [37]. The Dirac frequency is consequently plotted in Fig. 2 as a function of the normalized resonant frequency for

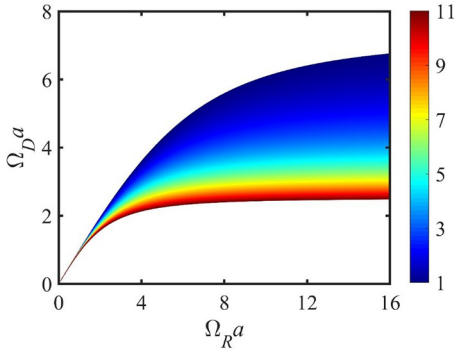

Fig. 2. The diagram of the normalized Dirac frequency $\Omega_D a$ as a function of the normalized resonant frequency $\Omega_\alpha a$ for different normalized mass γ_α values (denoted by the colour bar).

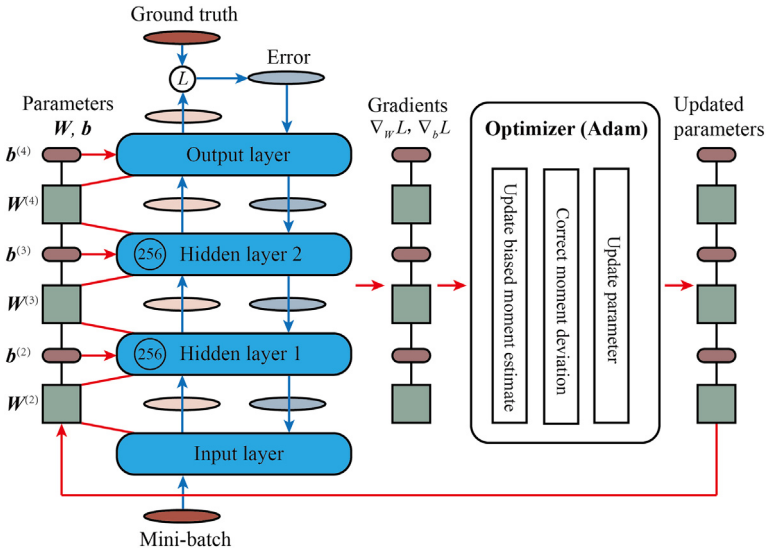

Fig. 3. Data flow cycle in the neural network during training (the forward propagation and backpropagation cycle in blue and optimization cycle in red). *L* represents the cost function. The ellipses between layers represent the intermediate results.

different normalized mass γ_α, indicated by the colour bar, which shows that γ_α runs from 1 to 10. Generally, increasing γ_α will decrease the Dirac frequency. On the other hand, the Dirac frequency converges then reaches to a limit when the normalized resonant frequency tends to infinite. This diagram provides full possibilities to design or inversely design the Dirac frequency as expected.

3. Prediction results and analysis of machine learning model

In this section, we establish a machine learning model for the forward and backward prediction of band gap. Machine learning algorithm can get the potential rules or characteristics behind the data so that it can be used to predict or make decisions on new data. The key points are the choice of model and the determination of model parameters. From an abstract point of view, machine learning algorithm can be described as determining a mapping function and its parameters to establish mapping relationship: $y = f(x; \theta)$. When the mapping function and parameters are determined, the output can be generated with given input. Artificial neural network algorithm is a typical representative of machine learning, a simplified model that established from the perspective of mathematical and physical methods and information processing. We can combine the PWE method and machine learning to study the application of machine learning algorithm in topological meta-plates for flexural wave manipulation.

We consider the red unit cell, which contains six resonators (see Fig. 1(a)). If the arrangement radius of resonators $R \neq a/3$, the double Dirac cone at Γ point in Fig. 1(c) will open and emerge a bandgap. To prepare the dataset for machine learning, we select 578 values of the parameter *R* covering from 8 mm to 20 mm linearly. By using the PWE method, we can obtain the dispersion curves for each value of *R*. Then we extract the bandgap information from the calculated dispersion curves, including the center frequency and bandgap width. Meanwhile, we record the value of *R* then use "0" and "1" to denote $R < a/3$ and $R > a/3$, respectively.

We build a neural network model with two hidden layers based on TensorFlow [39] to complete the regression task. Each hidden layer contains 256 neurons. The framework of data flow cycle in the neural network during the training is shown in Fig. 3. The bottom layer is the input layer which directly sends data to the next layer without any process. The top layer is the output layer after two hidden layers. The number of neurons in input layer and output layer is determined by the dimension of input vector and output vector. In the work of forward prediction band gap, the input information received by its input layer are 0/1 and center frequency, while bandgap width and arrangement radius *R* are the output of the model. In the further study of inverse design, we choose 0/1 and bandgap width as the input of the model and the output is the arrangement radius *R*. The calculation formula of any layer m of neural network is

$$\begin{cases} u^{(m)} = W^{(m)} x^{(m-1)} + b^{(m)} \\ x^{(m)} = f^{(m)} x^{(m-1)} = \phi\left(u^{(m)}\right) \end{cases} \quad 1 < m \le 4 \tag{11}$$

where $x^{(m-1)}$ is the output vector of layer *m*-1, $W^{(m)}$ represents the connection weight matrix of layer m and layer *m*-1, which size is $s_m \times s_{m-1}$, where s_m and s_{m-1} are the number of neurons in layer *m* and layer *m*-1, $b^{(m)}$ represents the bias in layer m, which is a column vector, and the Rectified Linear Unit (ReLU) is chosen as the activation function in

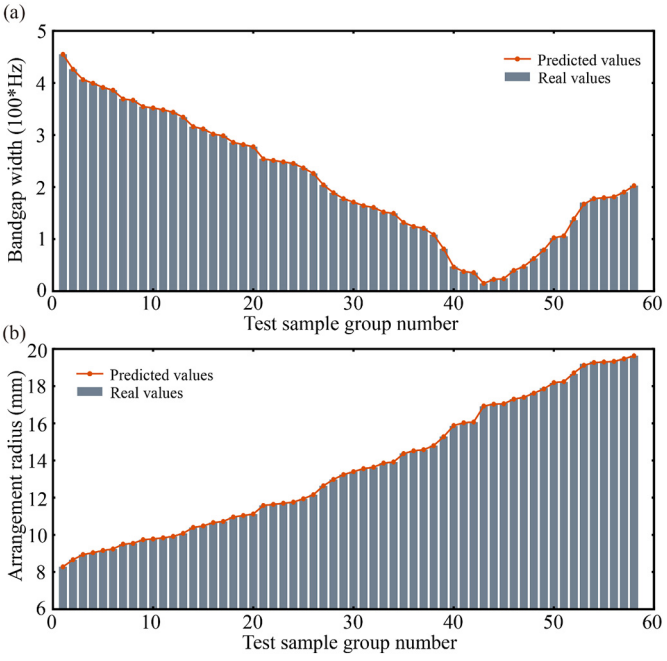

Fig. 4. Comparison between predicted value and real value for (a) prediction of bandgap width and (b) prediction of arrangement radius *R*.

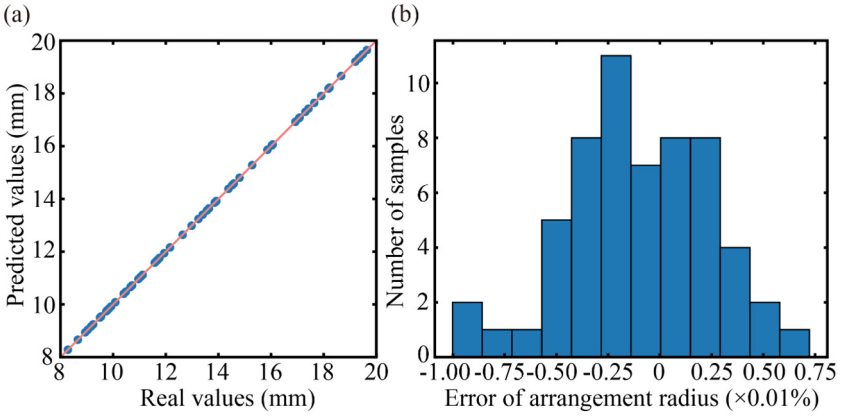

Fig. 5. (a) Comparison between the predicted value and the real value for the arrangement radius *R*. The orange solid line stands for the perfect same values in comparison. (b) Histogram of the prediction error, showing that the error is within 0.01%.

two hidden layers ($\phi(x) = \max(0,x)$), while linear output in the output layer ($\phi(x) = x$). Compared with other traditional activation functions, ReLU has the biological significance [40] with advantages such as the simplified calculation and avoiding the problem of gradient vanishing. According to Eq. (11), the feed forward propagation process of neural network from input layer to output layer can be described as

$$y = f\left(x^{(1)}\right) = f^{(4)} \circ f^{(3)} \circ f^{(2)}\left(x^{(1)}\right), \tag{12}$$

where ∘ is the symbol of function compound operation propagating between adjacent layers.

Backpropagation algorithm is a training algorithm suitable for multilayer neural networks. The purpose of training is to limit the prediction error of the final model to a reasonable range by gradually updating the weights and biases of each layer. The cost function is used to describe the prediction error as well as quantify the performance of the model. Mean square error (MSE) is one of the common cost functions which is chosen in this work. To reduce the cost of calculation and avoid large fluctuation of cost function, we can use a small part of all samples for each iteration which called Mini-batch. Define the MSE of single sample as $L_i = [f^{(4)} \circ f^{(3)} \circ f^{(2)}(x^{(1)}) - y^i]^2$. The traditional gradient descent algorithm is too sensitive to the hyperparameter of learning rate, where too low rate leads to slow convergence and too high rate will likely cross over the extreme point. Therefore, the dynamic updating strategy is adopted in this work. We use Adaptive Moment Estimation (Adam) as the optimizer (the detailed steps are given in Appendix A).

For the forward prediction model of band gap width, the training set accounts for 90% of the data set, while the testing set accounts for 10% in our work. After debugging, the batch size is set as 124, and the parameters in Adam optimizer include $\eta = 8e\text{-}5$, $\beta_1 = 0.99$, $\beta_2 = 0.99$ and $\varepsilon = 1e\text{-}8$. In order to avoid overfitting, the strategy of early termination is adopted. When epoch equals to 4317, we find sufficient good training results without overfitting or underfitting (see Appendix B). Then 58 groups of test samples are used to predict the values with the trained model.

We order the test sample group number as the increase of the arrangement radius *R*, then compare the predicted value (red dotted line) to the real value (grey vertical bar) for the bandgap width and arrangement radius in Fig. 4. Generally, the predicted values match quite well the real values as one can see the superposition of the red dot and the bar's top surface, proving the high accuracy of the trained model. Opening bandgaps from the double Dirac cones, one can notice that for a certain bandwidth, there are two *R* values which are smaller and larger than $a/3$, respectively.

Next, we consider using machine learning algorithm to predict two different arrangement radii for the same band gap which is an inverse prediction design. Compared with the aforementioned training, the batch size is set as 64, and the parameters in Adam optimizer are here changed to $\eta = 8e\text{-}7$, $\beta_1 = 0.99$, $\beta_2 = 0.99$ and $\varepsilon = 1e\text{-}8$. The early termination strategy fixed the training epoch in 3933. Similarly, we test the model with 58 groups of test samples after training the model. We plot the predicted values of *R* and the corresponding real values as the blue dots in Fig. 5(a) where the orange solid line stands for the perfect same values in correspondence. As seen in Fig. 5(a), all the blue dots locate on the orange line, showing a good performance in the inverse design. Fig. 5(b) shows that the prediction error for arrangement radius *R* is within 0.01% which indicates that given a bandgap width according to the practical needs, we can accurately obtain the corresponding *R* with this inverse prediction model.

4. Analysis of strip dispersion and eigenmodes

In the previous section, we considered the classical thin plate with honeycomb arrangement of resonators and developed a machine learning model which can inverse design the arrangement radius *R* for a given bandgap width. The double Dirac cones at Γ point shown in Fig. 1(c) can open to form a complete bandgap if *R* is changed different from $a/3$. When *R* sweeps around the critical value $a/3$, band inversion is found which supports a topological transition. Since the bandgaps for $R < a/3$ and $R > a/3$ have different topological phases, there will appear a topological edge state by combining two bulk media with the two respective *R* values. However, the quality of the topological edge state relates closely to the common bandgap width of these two-bulk media. If the common bandgap is too small, the topological edge state may not be excited owing to the poor energy confinement at the edge. Therefore, it's very important to inverse design the topological edge state with wide bandgaps.

The trained machine learning model in last section can instantaneous and precisely predict the arrangement radius *R* within 0.05 s if one inputs a required bandgap width. Now we choose 100 Hz and 230 Hz as the small and big bandgap widths, respectively. Then we obtain the corresponding predicted two pairs of *R*, as listed in Table 1. Since the prediction is highly precise as seen in Fig. 5, we directly plot the dispersion curves of flexural wave with these predicted two pairs of *R* and display in Fig. 6. The dispersions for $R < a/3$ and $R > a/3$ are marked as red triangles and blue solid lines, respectively, from which their common bandgaps are highlighted in orange. In each column of Fig. 6, the bands associated to the gap have different topological phases for $R < a/3$ and $R > a/3$, so that topological interface modes are possible

Table 1
Predicted *R* values by the trained machine learning model.

Bandgap width (Hz)	$R < a/3$ (mm)	$R > a/3$ (mm)
100	14.95	18.15
230	12.08	19.96

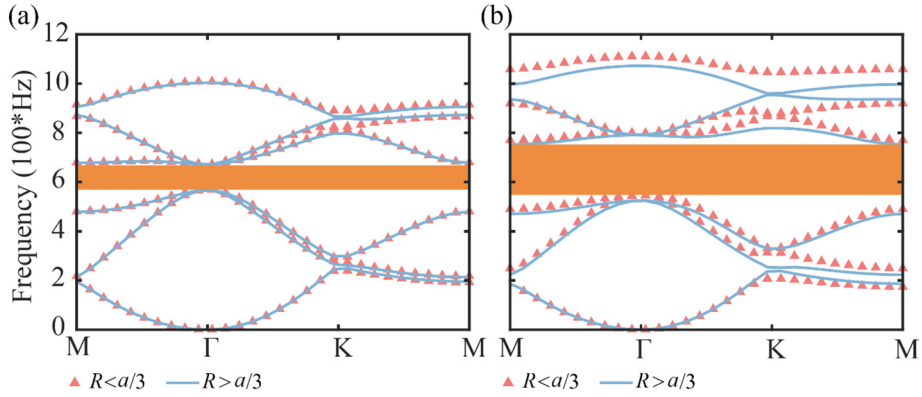

Fig. 6. Dispersion plot for (a) bandgap width = 100 Hz and (b) bandgap width = 230 Hz. The common bandgaps are highlighted as orange. The dotted and lined dispersions correspond to $R < a/3$ and $R > a/3$, respectively.

to appear when assembling the two bulk periodic media, for instance, two bulk media with $R = 18.15$ mm and 19.96 mm, respectively.

We now study the flexural wave eigenmode characteristics by strips for the cases of the bandgap width = 100 Hz and 230 Hz. We construct a supercell consisting of 5 units from both $R < a/3$ and $R > a/3$ lattice configurations adjacently as seen at the right panel of Fig. 7. As explained above, by assembling two bulk media with different topological phases, topologically protected edge modes can be designed in their common bandgap. The constructed supercell has 10 units length in y and periodic boundary conditions applied to the two edges in x to account for infinite length. We calculate the stripe's dispersions and plot in Fig. 7 where the black solid lines are the flexural wave dispersions of bare plate without any resonator. From both Fig. 7(a) and (b), we find a flat purple band appearing in the designed bandgap among the red bulk bands. We also present the eigenmodes of the purple band at $k_x a = \pi$ at the corresponding right panels, from which it reveals a topological edge mode around the interface separating the two bulk media. The topological edge mode in Fig. 7(b) with wider bandgap is more confined around the interface with less energy leakage into the bulk media than that with narrow bandgap in Fig. 7(a).

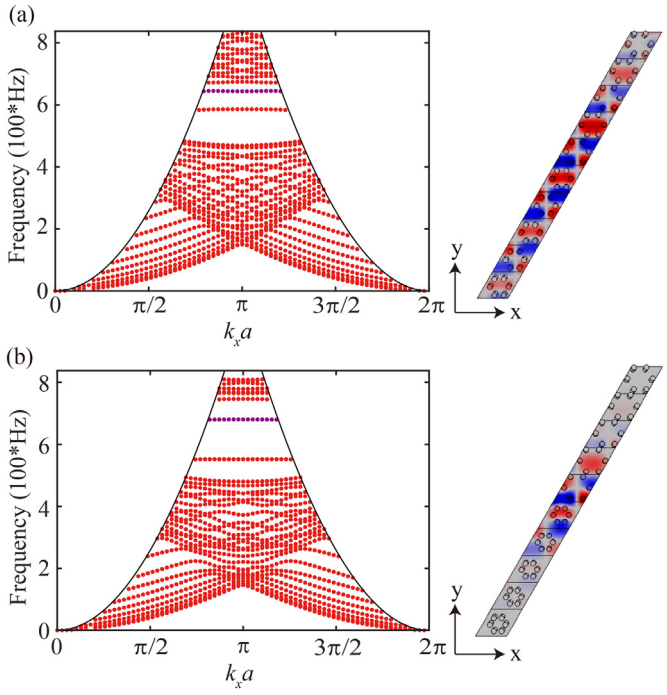

Fig. 7. Dispersion diagrams for strips and the eigenmodes at the purple flat edge band at $k_x a = \pi$ for (a) bandgap width = 100 Hz and (b) bandgap width = 230 Hz.

5. Designs of the topological edge states

To study the propagating property of the topological edge states, we construct a 16×16 supercell where the upper and lower half media correspond to $R < a/3$ (marked with S) and $R > a/3$ (marked with E), respectively. A point source is set at the left exit of the middle interface marked with a red star. We calculate the wave propagations with the MST method for the narrow and wide bandgap and display the wave propagating fields in Fig. 8(a) and (b), respectively. From the two displacement fields, clear edge states are found as expected. In Fig. 8(b) with the wide bandgap, the edge state can hardly penetrate the bulk media from the third unit away from the interface. However, the edge state in Fig. 8(a) with the narrow bandgap shows obvious wave leakage into the bulk media and the wave even passes through the upper whole media into the background plate. Due to the weak confinement, the edge state maximum amplitude is also lower in Fig. 8(a). In fact, if the initial designed bandgap width is further reduced, although a topological edge mode can still appear in the corresponding stripe dispersion, it can be barely excited with good quality in practice. The reason is that the edge state will widely spread in the whole supercell making the wave almost impossible to concentrate at the interface. The bandgap width dependent property reveals the importance to choose the bandgap width in design at the beginning properly. Therefore, the inverse design with the input bandgap width as needs by machine learning method provides an efficient strategy to realize topological states with C_{6v} lattices for great potential applications such as direction selective propagation, sensing, signal communication, energy harvesting.

We further design a cross type structure with the wide bandgap 230 Hz based on Fig. 8(b) to design direction-selective edge states as seen in Fig. 9. It should be noted that we use the multipoint sources to excite pseudospin directions by applying forces with different phases as shown by the enlarged unit cell at right with F_1, F_2 and F_3 from the red diamond. The gradient phases for the three point sources are $F_1 = F\exp(i\omega t)$, $F_2 = F\exp(i\omega t + 2\pi/3)$ and $F_3 = F\exp(i\omega t + \pi)$, respectively where the yellow arrow indicating the pseudospin direction and the frequency ω is 673.8 Hz. In Fig. 9, the lattice of $R > a/3$ (marked with E) is employed in the upper left and lower right while the lattice of $R < a/3$ (marked with S) is employed in the lower left and upper right. In Fig. 9(a), when the pseudospin direction is counter clockwise, the flexural wave is excited to propagate towards the right, then turn downward along the acute angle of the cross structure. In Fig. 9(b), with the clockwise direction, the excited edge state propagates towards the left then turns upward also along the acute angle. The cross-center parts are selected and displayed at right. One can see that the distance between the two "E" units in Fig. 9(a) or between the two "S" units in Fig. 9 is much shorter than that along the other diagonal line. This

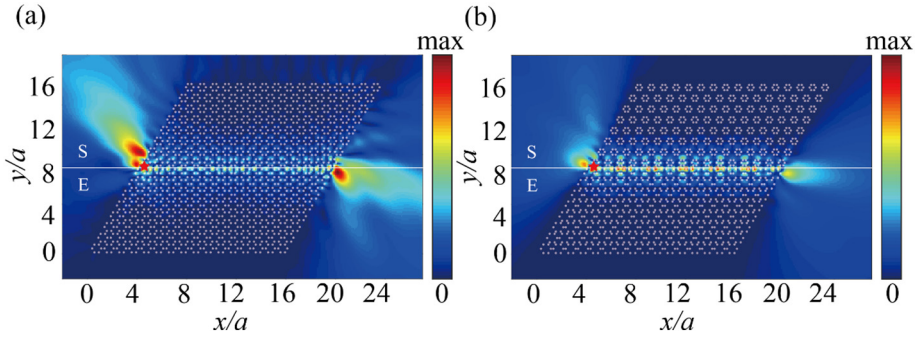

Fig. 8. Topological edge states with (a) narrow and (b) wide bandgaps along an interface separating expended (marked as E) and shrunken (marked as S) bulk media. The point source is excited at the left exit of the interface as marked by the red star.

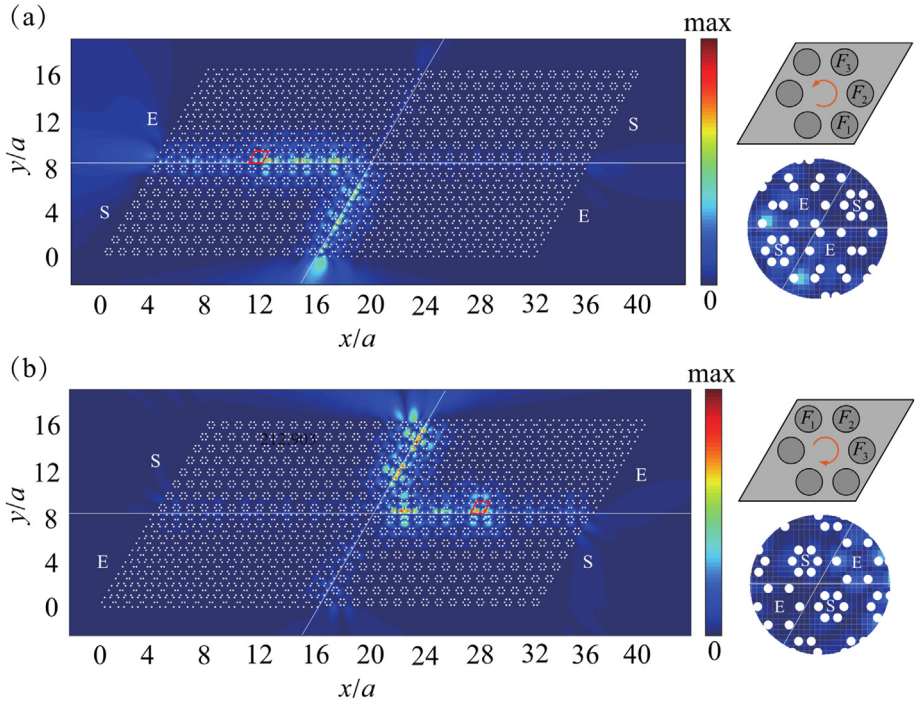

Fig. 9. MST simulation of direction selective topological edge states in cross structures with (a) counter clockwise (b) clockwise excitations in the red diamond unit, as the insets at right. The cross-center parts are also enlarged and displayed at right.

results in wave coupling in the "E-E" and "S-S" units through the obtuse angles which in turn guides the topological edge state along the acute angle without backscattering effect.

6. Summary

We realized an inverse design of topological edge states for flexural wave with machine learning method using the artificial neural network. The PWE method is used to analyze the band structures and the diagram of the Dirac frequency. By expending or shrinking the resonator's arrangements in the honeycomb unit, the Dirac cones can be opened and topological transition is enabled. Sweeping the arrangement radii, the generated data sets from the PWE method are used for training the feed forward artificial neural network, where the input are 0/1 (stands for shrink/expand) and center frequency of the opened bandgap while bandgap width and arrangement radius *R* are the output. Then the backward neural network is built by setting 0/1 and bandgap width as the input and the arrangement radius *R* as the output. The predicted results from both neural networks are highly accurate, showing that such inverse design scheme is helpful to directly link the bandgap characteristics with the geometric parameters through the complex nonlinear mapping relationship between them. By setting the bandgap width of 100 Hz and 230 Hz as the targets, the trained neural network allows us to accurately find out the resonator's arrangement radii that support topological transitions, which are further used to design topological edge states. From the comparison, the confinement of the topological edge state with wide bandgap is much better than that with narrow bandgap, making it possible to design more advanced functions such as direction selective propagation with sharp turns. The proposed machine learning inverse design of topological states for flexural wave is quite efficient with varied targets and has great potential applications such as signal processing with on-chip metamaterials [41], source direction sensing [42], and energy harvesting from vibration concentration [43].

Declaration of Competing Interest

The authors declare that they have no known competing financial interests or personal relationships that could have appeared to influence the work reported in this paper.

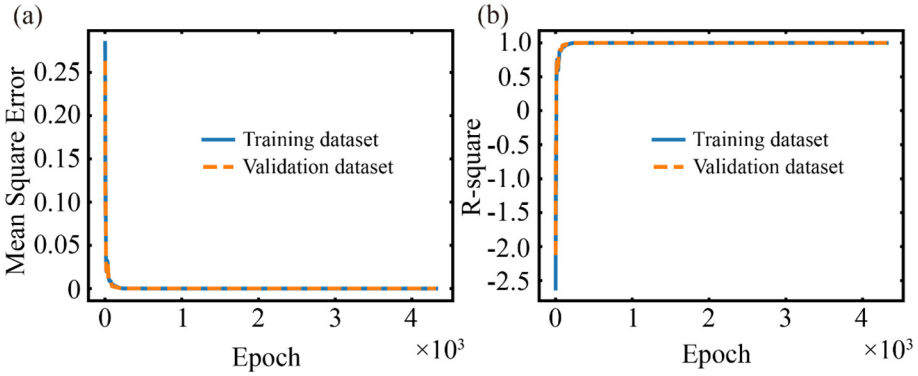

Fig. 10. The convergence history of the (a) mean squared error and (b) R-square for the forward model.

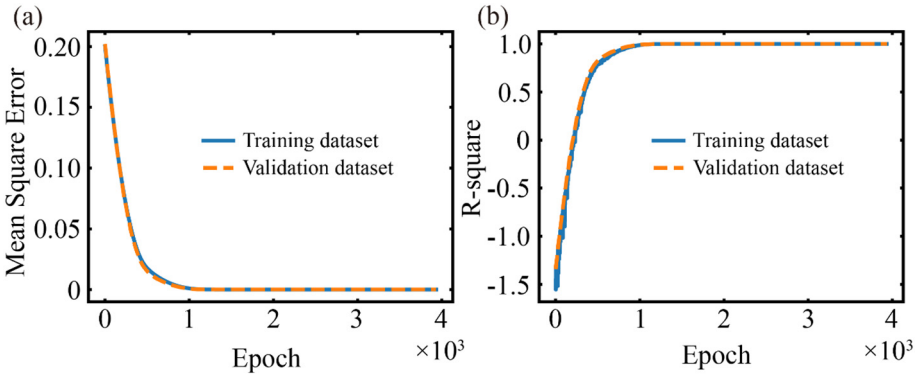

Fig. 11. The convergence history of the (a) mean squared error and (b) R-square for the inverse model.

Acknowledgment

This work is supported by the National Natural Science Foundation of China (11902223), the Shanghai Pujiang Program (19PJ1410100), the program for professor of special appointment (Eastern Scholar) at Shanghai Institutions of Higher Learning, the Fundamental Research Funds for the Central Universities and Shanghai municipal peak discipline program (2019010106). The authors would like to thank Dr. Hongwei Guo for fruitful discussions.

Appendix A. The operation steps of Adam optimizer

The Adam optimizer which is used in the back propagation can be organized as initialize the first and second moment variables $s = 0$, $r = 0$, and suppose the gradient of the $t + 1$th iteration is

$$g_{t+1} = \frac{1}{\text{batch\_size}} \sum_{i=j}^{j+\text{batch\_size}} \nabla_\theta L\left(f\left(x^i,\ \theta_t\right),\ y^i\right), \tag{13}$$

where θ contains weights and biases. By combine the Eq. (11), we can get the gradient of the cost function to the parameter is

$$\begin{cases} \nabla_{W^{(m)}} L = \left(\nabla_{u^{(m)}} L\right)\left(x^{(m-1)}\right)^{\mathrm{T}}, \\ \nabla_{b^{(m)}} L = \nabla_{u^{(m)}} L. \end{cases} \tag{14}$$

If layer m is the output layer, then $\nabla_{u^{(m)}} L = (\nabla_{x^{(m)}} L) \odot \phi'(u^{(m)}) = (x^{(m)} - y) \odot \phi'(u^{(m)})$, else if layer m is hidden layer, then $\nabla_{u^{(m)}} L = (\nabla_{x^{(m)}} L) \odot \phi'(u^{(m)}) = [(W^{(m+1)})^{\mathrm{T}}]$, where $\odot$ represents the Hadamard product. The error term is defined as the gradient of cost function to temporary variable u

$$\delta^{(m)} = \nabla_{u^{(m)}} L = \begin{cases} \left(x^{(m)} - y\right) \odot \phi'\left(u^{(m)}\right) & m = 4, \\ \left(w^{(m+1)}\right)^{\mathrm{T}} \left(\delta^{(m+1)}\right) \odot \phi'\left(u^{(m)}\right) & m \neq 1, 4. \end{cases} \tag{15}$$

Substituting Eq. (15) into (14), the gradient of the cost function to the weights and biases can be obtained. For each iteration, we can get the total average gradient by Eq. (13). And then, Computing the biased first-order moment estimation $s_{t+1} = \beta_1 s_t + (1 - \beta_1) g_{t+1}$ and biased second moment estimation $r_{t+1} = \beta_2 r_t + (1 - \beta_2) g_{t+1}^2$, where β_1 and β_2 are exponential decay rate of moment estimation. The moment deviation is corrected as $\hat{s} = \frac{s}{1-\beta_1^{t+1}}$ and $\hat{r} = \frac{r}{1-\beta_2^{t+1}}$. Finally, the parameter updating rules of Adam follow

$$\theta_{t+1} = \theta_t - \eta \frac{\hat{s}}{\sqrt{\hat{r}} + \varepsilon} \tag{16}$$

where η denotes the learning rate and ε is a small parameter to avoid zero denominator.

Appendix B. The overfitting or underfitting judgment of the two models

We take 10% of the samples from the training set as the validation dataset and plot the trend of MSE and R-square during the training process in Figs. 10 and 11, respectively. The difference between the validation and training losses is small (see Figs. 10(a) and 11(a)) which show that both the forward and inverse prediction model are no significant

overfitting or underfitting. While the R-square are gradually approaching 1.0 (see Figs. 10(b) and 11(b)) which indicate that the models fit the data well.

References

[1] M.Z. Hasan, C.L. Kane, Colloquium: topological insulators, Rev. Mod. Phys. 82 (2010) 3045–3067.
[2] C.L. Kane, E.J. Mele, Quantum spin hall effect in graphene, Phys. Rev. Lett. 95 (2005) 4.
[3] B.A. Bernevig, T.L. Hughes, S.C. Zhang, Quantum spin hall effect and topological phase transition in HgTe quantum wells, Science 314 (2006) 1757–1761.
[4] T. Ma, G. Shvets, All-Si valley-Hall photonic topological insulator, New J. Phys. 18 (2016) 9.
[5] L. Lu, J.D. Joannopoulos, M. Soljacic, Topological photonics, Nat. Photonics 8 (2014) 821–829.
[6] M. Hafezi, S. Mittal, J. Fan, A. Migdall, J.M. Taylor, Imaging topological edge states in silicon photonics, Nat. Photonics 7 (2013) 1001–1005.
[7] W.L. Gao, M. Lawrence, B.A. Yang, F. Liu, F.Z. Fang, B. Beri, J.S. Li, S. Zhang, Topological photonic phase in chiral hyperbolic Metamaterials, Phys. Rev. Lett. 114 (2015) 5.
[8] T. Stauber, G. Gómez-Santos, L. Brey, Plasmonics in topological insulators: spin–charge separation, the influence of the inversion layer, and Phonon–Plasmon coupling, ACS Photonics 4 (2017) 2978–2988.
[9] S.R. Pocock, X. Xiao, P.A. Huidobro, V. Giannini, Topological plasmonic chain with retardation and radiative effects, ACS Photonics 5 (2018) 2271–2279.
[10] C. He, X. Ni, H. Ge, X.C. Sun, Y.B. Chen, M.H. Lu, X.P. Liu, Y.F. Chen, Acoustic topological insulator and robust one-way sound transport, Nat. Phys. 12 (2016) 1124-+.
[11] Z.J. Yang, F. Gao, X.H. Shi, X. Lin, Z. Gao, Y.D. Chong, B.L. Zhang, Topological acoustics, Phys. Rev. Lett. 114 (2015) 4.
[12] Z.W. Zhang, Q. Wei, Y. Cheng, T. Zhang, D.J. Wu, X.J. Liu, Topological creation of acoustic pseudospin multipoles in a flow-free symmetry-broken metamaterial lattice, Phys. Rev. Lett. 118 (2017) 6.
[13] R. Fleury, A.B. Khanikaev, A. Alu, Floquet topological insulators for sound, Nat. Commun. 7 (2016) 11.
[14] W. Wang, Y. Jin, W. Wang, B. Bonello, B. Djafari-Rouhani, R. Fleury, Robust Fano resonance in a topological mechanical beam, Phys. Rev. B 101 (2020) 024101.
[15] Y. Jin, W. Wang, B. Djafari-Rouhani, Asymmetric topological state in an elastic beam based on symmetry principle, Int. J. Mech. Sci. 186 (2020) 105897.
[16] Y. Jin, D. Torrent, B. Djafari-Rouhani, Robustness of conventional and topologically protected edge states in phononic crystal plates, Phys. Rev. B 98 (2018) 054307.
[17] Y. Jin, B. Djafari-Rouhani, D. Torrent, Gradient index phononic crystals and metamaterials, Nanophotonics 8 (2019) 685.
[18] R.K. Pal, M. Ruzzene, Edge waves in plates with resonators: an elastic analogue of the quantum valley Hall effect, New J. Phys. 19 (2017) 025001.
[19] R. Chaunsali, C.-W. Chen, J. Yang, Subwavelength and directional control of flexural waves in zone-folding induced topological plates, Phys. Rev. B 97 (2018) 054307.
[20] Y. Jin, W. Wang, Z. Wen, D. Torrent, B. Djafari-Rouhani, Topological states in twisted pillared phononic plates, Extreme Mech. Lett. 39 (2020) 100777.
[21] H.-W. Dong, S.-D. Zhao, R. Zhu, Y.-S. Wang, L. Cheng, C. Zhang, Customizing acoustic Dirac cones and topological insulators in square lattices by topology optimization, J. Sound Vib. (2020) 115687, https://doi.org/10.1016/j.jsv.2020.115687.
[22] S.S. Nanthakumar, X. Zhuang, H.S. Park, C. Nguyen, Y. Chen, T. Rabczuk, Inverse design of quantum spin hall-based phononic topological insulators, J. Mech. Phys. Solids 125 (2019) 550–571.
[23] Z. Wang, A. Sobey, A comparative review between genetic algorithm use in composite optimisation and the state-of-the-art in evolutionary computation, Compos. Struct. 233 (2020) 111739.
[24] K. Gopalakrishnan, 3 - particle swarm optimization in civil infrastructure systems: State-of-the-art review, in: A.H. Gandomi, X.-S. Yang, S. Talatahari, A.H. Alavi (Eds.), Metaheuristic Applications in Structures and Infrastructures, Elsevier, Oxford 2013, pp. 49–76.
[25] K. Yao, R. Unni, Y. Zheng, Intelligent nanophotonics: merging photonics and artificial intelligence at the nanoscale, Nanophotonics 8 (2019) 339.
[26] Y. Kiarashinejad, S. Abdollahramezani, M. Zandehshahvar, O. Hemmatyar, A. Adibi, Deep learning reveals underlying physics of light–matter interactions in nanophotonic devices, Adv. Theory Simul. 2 (2019) 1900088.
[27] I. Malkiel, M. Mrejen, A. Nagler, U. Arieli, L. Wolf, H. Suchowski, Deep learning for the design of nano-photonic structures, 2018 IEEE International Conference on Computational Photography (ICCP) 2018, pp. 1–14.
[28] W. Ma, F. Cheng, Y. Liu, Deep-learning-enabled on-demand design of chiral metamaterials, ACS Nano 12 (2018) 6326–6334.
[29] I. Malkiel, M. Mrejen, A. Nagler, U. Arieli, L. Wolf, H. Suchowski, Plasmonic nanostructure design and characterization via deep learning, Light: Sci. Applic. 7 (2018) 60.
[30] L. Li, H. Ruan, C. Liu, Y. Li, Y. Shuang, A. Alù, C.-W. Qiu, T.J. Cui, Machine-learning reprogrammable metasurface imager, Nat. Commun. 10 (2019) 1082.
[31] B. Orazbayev, R. Fleury, Far-field subwavelength acoustic imaging by deep learning, Phys. Rev. X 10 (2020) 031029.
[32] C. Luo, S. Ning, Z. Liu, Z. Zhuang, Interactive inverse design of layered phononic crystals based on reinforcement learning, Extreme Mech. Lett. 36 (2020) 100651.
[33] Y. Long, J. Ren, H. Chen, Unsupervised manifold clustering of topological phononics, Phys. Rev. Lett. 124 (2020) 185501.
[34] H. Guo, X. Zhuang, T. Rabczuk, A deep collocation method for the bending analysis of kirchhoff plate, Comput. Mater. Continua 59 (2019) 433–456.
[35] E. Samaniego, C. Anitescu, S. Goswami, V.M. Nguyen-Thanh, H. Guo, K. Hamdia, X. Zhuang, T. Rabczuk, An energy approach to the solution of partial differential equations in computational mechanics via machine learning: concepts, implementation and applications, Comput. Methods Appl. Mech. Eng. 362 (2020) 112790.
[36] H. Guo, H. Zheng, X. Zhuang, Numerical manifold method for vibration analysis of Kirchhoff's plates of arbitrary geometry, Appl. Math. Model. 66 (2019) 695–727.
[37] D. Torrent, D. Mayou, J. Sánchez-Dehesa, Elastic analog of graphene: Dirac cones and edge states for flexural waves in thin plates, Phys. Rev. B 87 (2013) 115143.
[38] Y. Xiao, J. Wen, X. Wen, Flexural wave band gaps in locally resonant thin plates with periodically attached spring–mass resonators, J. Phys. D. Appl. Phys. 45 (2012) 195401.
[39] M. Abadi, A. Agarwal, P. Barham, E. Brevdo, Z. Chen, C. Citro, G.S. Corrado, A. Davis, J. Dean, M. Devin, S. Ghemawat, I. Goodfellow, A. Harp, G. Irving, M. Isard, Y. Jia, R. Jozefowicz, L. Kaiser, M. Kudlur, J. Levenberg, D. Mane, R. Monga, S. Moore, D. Murray, C. Olah, M. Schuster, J. Shlens, B. Steiner, I. Sutskever, K. Talwar, P. Tucker, V. Vanhoucke, V. Vasudevan, F. Viegas, O. Vinyals, P. Warden, M. Wattenberg, M. Wicke, Y. Yu, X.J.A.E.-P. Zheng, TensorFlow: Large-Scale Machine Learning on Heterogeneous Distributed Systems, arXiv:1603.04467 2016.
[40] X. Glorot, A. Bordes, Y. Bengio, Deep sparse rectifier neural networks, 14th International Conference on Artificial Intelligence and Statistics, AISTATS 2011, April 11, 2011–April 13, 2011, Microtome Publishing, Fort Lauderdale, FL, United States 2011, pp. 315–323.
[41] J. Cha, K.W. Kim, C. Daraio, Experimental realization of on-chip topological nanoelectromechanical metamaterials, Nature 564 (2018) 229–233.
[42] T. Jiang, C. Li, Q. He, Z.-K. Peng, Randomized resonant metamaterials for single-sensor identification of elastic vibrations, Nat. Commun. 11 (2020) 2353.
[43] C.-S. Park, Y.C. Shin, S.-H. Jo, H. Yoon, W. Choi, B.D. Youn, M. Kim, Two-dimensional octagonal phononic crystals for highly dense piezoelectric energy harvesting, Nano Energy 57 (2019) 327–337.